Journal of Advanced Ceramics
2019, **8**(2): 174–185
https://doi.org/10.1007/s40145-018-0303-3
ISSN 2226-4108
CN 10-1154/TQ

Research Article

Dielectric relaxation and magneto-electric characteristics of lead-free double perovskite: Sm_2NiMnO_6

Rutuparna DAS*, R. N. P. CHOUDHARY

Department of Physics, Siksha 'O' Anusandhan University, Bhubaneswar 751030, India

Received: June 9, 2018; Revised: November 5, 2018; Accepted: November 8, 2018

Abstract: The polycrystalline sample of a double perovskite, Sm_2NiMnO_6 was synthesized by a solid-state reaction route. From the X-ray structural study, it is found that the structure of the material is monoclinic with lattice parameters: a = 4.1750(63) Å, b = 7.6113(63) Å, c = 5.9896(63) Å, and β = 112.70°. These parameters are very close to and consistent with those of such type of materials. The dielectric, impedance, AC conductivity, and electrical modulus properties of the sample were studied in the temperature range of 25–300 ℃ and the frequency range of 1 kHz–1 MHz. Typical relaxor behavior observed in the dielectric studies was confirmed by Vogel–Fulcher fitting. From the Nyquist plots, the temperature dependent contribution of grain and grain boundary effect was confirmed. The non-Debye type of relaxation was found using the complex impedance spectroscopy. The magnetic study revealed that the sample had paramagnetic behavior at room temperature. Magneto-electric (ME) coefficient was obtained by changing DC bias magnetic field. This type of lead-free relaxor ferroelectric compound may be useful for high-temperature applications.

Keywords: solid-state reaction; X-ray diffraction (XRD); dielectric relaxation; magneto-electric (ME) coupling

1 Introduction

Multiferroics are a special class of advanced materials. Such type of materials has more than one primary ferroic order parameters. They are challenging and exciting materials because of their multifunctional applications, such as sensors, transducers, memories, and spintronics. For practical applications of multiferroics, it is a great challenge to achieve the existence of magneto-electric (ME) coupling [1] in the materials. They exhibit different properties, such as insulating, metallic, ferromagnetic, ferroelectric, magneto-dielectric, multiferroic, etc. [2]. Ferroelectric and ferromagnetic materials have been broadly studied due to their vital scientific and technological advances. The ordering of charge, octahedral distortion, strain mediation, lone-pair of electron, and geometrical frustration are the main source for ferroelectricity in the material and an empty d-orbital is needed. In a ferromagnetic material, the origin of magnetism is associated with the spin ordering, and it requires half filled d-orbital. Ferroelectric materials are used in fabrication of capacitors having large dielectric constant, transducers actuators, and their memory applications. Likewise, ferromagnetic materials are applicable for various applications like sensors, read heads, and memories depending on giant magnetoresistive analysis [3]. As single-phase compounds

* Corresponding author.
E-mail: rutulucy2013@gmail.com

occur frequently in environment having such cross-coupling characteristics, a rigorous investigation followed to find the novel single-phase multiferroic compound and developed novel materials having ME coupling. The double perovskites of a general formula $A_2B'B''O_6$ (A is an alkaline-earth or rare-earth element, B′ and B″ are transition-metal elements) have drawn a large attention for the researchers owing to their exclusive electrical and magnetic properties. The structure of double perovskite materials may also be imagined from tolerance factor. The tolerance factor (t) can be determined by a general formula:

$$t = \frac{r_A + r_O}{\sqrt{2}\left[\left(\frac{r_{B'} + r_{B''}}{2}\right) + r_O\right]}$$

where r_A, $r_{B'}$, $r_{B''}$, and r_O are the ionic radii of A, B′, and B″ cations and oxygen anion, respectively [4,5]. The strength of double perovskite compounds depends on B′ and B″ cations distribution over the octahedral sites, degree of the cation inversion, the size, and electronic structure of the transition metal cations of B′ and B″. R_2NiMnO_6 (R represents rare earth) series belong to a specific catagory of double perovskite oxides. In such type of materials, the Ni^{2+}–O–Mn^{4+} interactions would yield new information about the fabrication of multi-property materials [6]. As ferromagnetic interaction arises due to the arrangement of Ni–O–Mn, it is considered as a promising candidate for multifunctional applications. As such, in current time, it has been shown that besides the ferromagnetism, the existence of giant dielectric characteristics and magneto resistance, is owing to the Ni^{3+}–O–Mn^{3+} super-exchange interactions. Reshak and Azam [7] showed that the ferromagnetism is totally due to the Ni^{2+}–O–Mn^{4+} super-exchange interactions. The giant dielectric constant in such type of materials is the consequence of charge ordering between Ni^{2+} and Mn^{4+} [8]. As MnO_2 is the best suitable additive, it is commonly used to fabricate such type of double perovskite because of its multi-valencies: Mn^{2+}, Mn^{3+}, and Mn^{4+}. Therefore, the rare earth and manganese element containing double perovskites may be used for various device applications. The double perovskite materials with transition metal have drawn much more attention in different technical fields, practical and primary areas of material science, as a consequence of its prominent characteristics like ME [9,10].

In the view of the significance of the multifunctional materials, the preparation and characterization of a double perovskite, Sm_2NiMnO_6, were carried out using various experimental procedures as a function of frequency and temperature. In this study, we have analyzed structural, microstructural, dielectric, electric, magnetic, and magnetoelectric characteristics of the material. We have found the relaxor ferroelectric nature of the sample. Most of the relaxor ferroelectrics are complex perovskite structure having fully or partially disorders among two or more ions in the A- and B-sub-lattice of the perovskite (ABO_3) structure [11]. This material may be useful for various industrial applications including non-volatile memories, capacitors, sensors, actuators, resonant wave devices (such as radio-frequency filters), infra-red detectors, optical switches, and electric-motor overload protection circuits with multiple function, making them more attractive [12]. In addition, the diffused phase transition with the relaxor behavior of the material is discussed in great details.

2 Experimental

Sm_2NiMnO_6 polycrystalline material was synthesized by using a solid-state reaction method taking pure ingredients Sm_2O_3 (>99.9%), MnO_2 (M/S Loba Chemie Co.), and NiO (M/S Himedia) in a proper stoichiometry. The homogeneous mixture of these oxide powders was obtained by both dry and wet (by methanol) grinding using agate mortar and pestle. To get required material, the mixture of ingredients was fired at several temperatures to follow the ceramic technology (i.e., repeated fining and grinding of the sample). Finally, the mixture was calcined at 1200 ℃. The powder was further ground after calcination. The room-temperature XRD pattern of powder sample was obtained by X-ray powder diffractometer with Cu Kα radiation (wavelength = 1.5406 Å) in a wide range of Bragg's angle ($20° \leqslant 2\theta \leqslant 80°$). To prepare pellets, a binder (polyvinyl alcohol (PVA)) was used. Then pellets were fabricated in the cylindrical shape of diameter 12 mm and thickness 1.65 mm under the pressure of 4×10^6 N·m^{-2} by a KBR hydraulic press. The pellets were sintered at 1250 ℃ in atmospheric air for 4 h. The micrograph of a sintered pellet was recorded by a scanning electron microscope (SEM, Inspect-S50). Both sides of the pellet were painted with conducting silver paste, and afterwards heated at 150 ℃ for 45 min before electric and dielectric measurements. By using an LCR meter (N4L PSM, 1735), dielectric constant (ε_r), tangent loss ($\tan\delta$),

impedance, conductance, etc., of the material were obtained in a certain frequency range of 1 kHz–1 MHz and the temperature range of 25–300 ℃ range, and the magneto-electric coefficient was studied at room temperature using ME setup (M/S Marine India). In the ME setup, the maximum 7 kOe DC magnetic field was developed by means of the electromagnet, and the AC magnetic field was created from a Helmholtz coil (200 turns and radius = 2.5 cm). The room temperature *M–H* loop was obtained using a vibrating sample magnetometer (VSM LAKESHORE-7410) with a maximum magnetic field up to 20,000 G.

3 Results and discussion

3. 1 Structural studies

Depending on the value of tolerance factor (t), the structure of the double perovskite materials can be explained. From Ref. [6], it is found that double perovskite materials have a cubic structure, if $1.05 > t > 1.00$, but for $1.00 > t > 0.97$, the materials exhibit tetragonal structure. For $t < 0.97$, the structure will be either orthorhombic or monoclinic. We also find that the tolerance factor of Sm_2NiMnO_6 (SNMO) is less than 0.97, which indicates that there is a structural distortion from cubic symmetry. The XRD pattern of Sm_2NiMnO_6 is shown in Fig. 1(a). The indexing of the peaks was done in both orthorhombic and monoclinic systems using "POWD MULT" software and the structure of SNMO was obtained as a single phase monoclinic structure (distorted double-perovskite) with the lattice parameters: a = 4.1750(63) Å, b = 7.6113(63) Å, c = 5.9896(63) Å, β = 112.70°, and V = 175.58 (Å)^3. The obtained lattice parameters are close in Ref. [5] to those for Sm_2NiMnO_6. All the peaks with d_{obs}, d_{cal}, and (h k l) values are given in Table 1. The crystallite size (D) has been estimated by Scherrer's formula with the full width half maximum (β of the diffraction peak; $D = \dfrac{k\lambda}{\beta_{1/2}\cos\theta}$ (λ = X-ray wavelength (0.15406 nm), θ = diffraction angle, k = 0.89). Thus, the calculated value of D was found to be 65 nm. Figure 1(b) shows the image of the room-temperature microstructure of the sintered pellets. The image shows the different size of grains, which are scattered homogeneously with small voids suggesting the polycrystalline nature of the material. The size of grains was in the range of 0.9–2.2 μm.

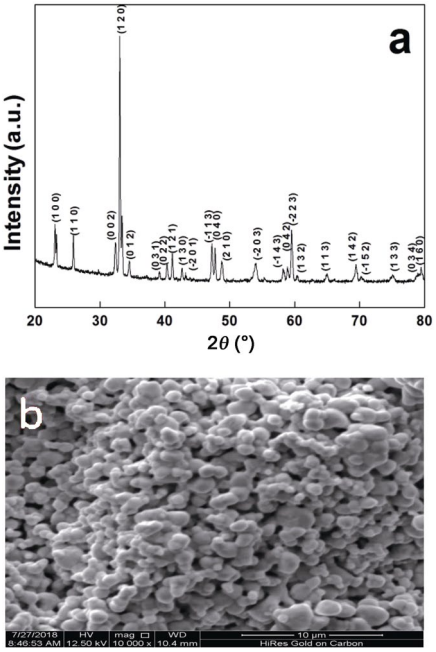

Fig. 1 (a) Room-temperature XRD pattern and (b) SEM image of Sm_2NiMnO_6.

Table 1 Comparison of observed d_{obs} and calculated d_{Cal}, and d values of Sm_2NiMnO_6 with relative intensities I/I_0

SL. No.	d_{obs}(Å)	D_{cal}(Å)	h	k	l	I/I_0
1	3.8470	3.8515	1	0	0	30
2	3.4345	3.4365	1	1	0	20
3	2.7609	2.7627	0	0	2	20
4	2.7056	2.7071	1	2	0	100
5	2.5960	2.5969	0	1	2	10
6	2.2996	2.3057	0	3	1	10
7	2.2328	2.2357	0	2	2	10
8	2.1902	2.2060	1	2	1	10
9	2.1167	2.1187	1	3	0	10
10	2.0924	2.0858	–2	0	1	10
11	1.9217	1.9222	–1	1	3	20
12	1.9034	1.9028	0	4	0	20
13	1.8660	1.8669	2	1	0	10
14	1.6943	1.6981	–2	0	3	10
15	1.5833	1.5771	–1	4	2	10
16	1.5666	1.5671	0	4	2	10
17	1.5513	1.5507	–2	2	3	20
18	1.5322	1.5315	1	3	2	10
19	1.4344	1.4311	1	1	3	10
20	1.3520	1.3519	1	4	2	10
21	1.3396	1.3394	–1	5	2	10
22	1.2636	1.2635	1	3	3	10
23	1.2127	1.2132	0	3	4	10
24	1.2046	1.2049	1	6	0	10

3. 2 Dielectric studies

By the influence of AC electric field, the dielectric study of the compound can be explained by the complex permittivity having both real and imaginary parts, such as

$$\varepsilon^* = \varepsilon' + i\varepsilon'' \quad (1)$$

where ε' (dielectric constant) signifies the energy stored and ε'' ($\tan\delta$) is the energy loss during every cycle of electric field. The temperature dependence of relative dielectric constant (ε_r) and tangent loss ($\tan\delta$) at some certain frequencies of the material have been shown in Fig. 2. From Fig. 2(a), it is pointed out that the value of dielectric constant remains the same nearly up to 60 ℃, and then rises with the enhancement of temperature. There is an occurrence of an anomaly near 200 ℃, and then the value abruptly reduces. The systematically shifting of peaks in the direction of high temperature by the enhancement of frequency represents dielectric relaxation. In the low-temperature region (Fig. 2(b)), the $\tan\delta$ value is low,

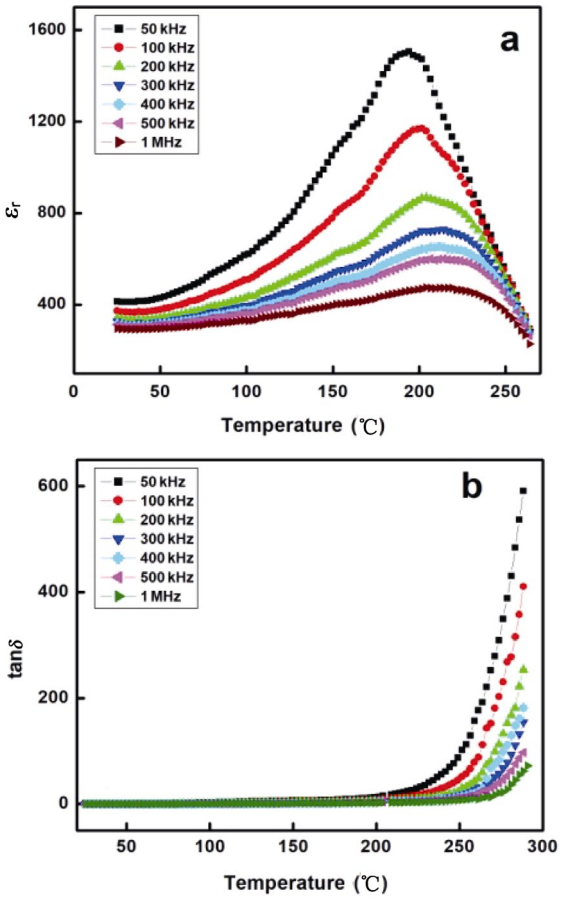

Fig. 2 (a) Variation of relative dielectric constant and (b) $\tan\delta$ with temperature at some selected frequencies.

but with the enhancement of temperature, it rises suddenly to a large value. This happens as the result of scattering of thermally stimulated charge carriers and defect in the sample, which is also studied by SEM analysis. At high temperature, the dominating character of conductivity causes increase in $\tan\delta$ [13]. This result is analogous with the data given for same type of compounds. The obtained dielectric permittivity value of Sm_2NiMnO_6 is analogous to that reported earlier, where the dielectric constant is ~1500 [14] and the room-temperature $\tan\delta < 10$. Shi *et al*. [15] discussed for a similar type of the material (Nd_2NiMnO_6).

3. 3 Dielectric relaxation

Relaxation corresponds to the monotonous approach of the system to the stable state after some excitation. The relaxor nature is understood by the survival of polar nano-regions (PNRs), which acquire dissimilar relaxation time. The relaxation time (τ) corresponds to the response of the time of such PNRs with the variation of the applied electric field. However, this phenomenon does not happen spontaneously. In fact, the existence of some inertia may be the origin of the dielectric relaxation in relaxor ferroelectrics. The PNRs occur at a particular temperature named as the Burns' temperature (T_B), which is normally hundreds of degrees more than the maximum temperature (T_m) of real dielectric permittivity. Relaxor ferroelectrics are a group of disordered crystals possessing irregular structure and characteristics [16,17]. Relaxor ferroelectrics are characterized by broad peak with relaxation dispersion in the temperature dependent dielectric permittivity curve [18]. Such nature is noticed in the studied material that induced by several logics via a microscopic composition variation. It is because of coinciding of multiple micropolar regions into a single macropolar region, or a combination of ordering parameter and local disorder mode via the local strain. It is also discussed that the arbitrarily dispersed electrical field of strain field in a mixed oxide system is the major cause of the relaxor behavior in Ref. [19]. The ferroelectric diffused phase transition is described by a temperature of maximum permitivity (T_m) which does not depend on frequency, while a relaxor ferroelectric is found to have a frequency-dependent T_m satisfying Vogel–Fulcher relation [20]. For normal ferroelectrics, dielectric constant must obey the Curie–Weiss law,

which is given by $\varepsilon = C/(T - T_0)$ (T_0 = Curie–Weiss temperature, C = Curie–Weiss constant). In Fig. 2(a), the occurrence of wide peaks (with diffused phase transition) is the main characteristic of relaxor ferroelectric. In such situation, at low temperature, the frequency dispersion in permittivity is found, whereas, the high temperature permittivity is almost frequency independent. This kind of relaxer behavior may be illustrated by modified Curie–Weiss law. This is defined as

$$\frac{1}{\varepsilon}-\frac{1}{\varepsilon_{\mathrm{m}}}=\frac{\left(T-T_{\mathrm{m}}\right)^{\gamma}}{C} \quad \text{or}$$

$$\ln\left(\frac{1}{\varepsilon}-\frac{1}{\varepsilon_{\mathrm{m}}}\right)=\gamma\ln\left(T-T_{\mathrm{m}}\right)-\ln C \qquad (2)$$

where C is the Curie constant and T_{m} is the temperature corresponding to maximum dielectric permittivity (ε_{m}). The diffusion co-efficient (γ) or diffusivity ranges from 1 (normal ferroelectric) to 2 (relaxor ferroelectric). Figure 3 displays the graph between $\ln\left(\frac{1}{\varepsilon}-\frac{1}{\varepsilon_{\mathrm{m}}}\right)$ and $\ln(T-T_{\mathrm{m}})$. From the linear relation, the slope of thefitting curve will give the γ value. It is observed that the γ value rises from 1.69 to 1.81 with an increase in frequency. So, we can conclude that the diffuseness rises with the enhancement of frequency. The relaxor ferroelectrics can also be described by Vogel–Fulcher law:

$$f = f_0\exp\left[\frac{-E_{\mathrm{a}}}{k\left(T-T_{\mathrm{f}}\right)}\right] \qquad (3)$$

where f, f_0, k, and E_{a} are operating frequency, pre-exponential factor, Boltzmann constant, and the activation energy, respectively. T_{f} (freezing temperature) is the temperature at which dynamic reorientation of the dipolar cluster polarization can no longer be thermally activated. Figure 4 shows the graph of ln$f$ with inverse temperature (T_{m}). The activation energy (E_{a} = 0.386 eV), pre-exponential factor ($f_0 = 1.3 \times 10^6$ Hz), and freezing temperature (T_{f} = 127 ℃) were calculated from Vogel–Fulcher law fitting (R^2 = 0.9958). From the value of E_{a}, the degree of the relaxing nature can be understood, i.e., the larger the value of E_{a}, the larger the strength of the relaxing nature. The necessary energy for the movement of an electron from Ni^{+2} to Mn^{+4} is close to this determined activation energy. Thus relaxor nature of the compound was proved from

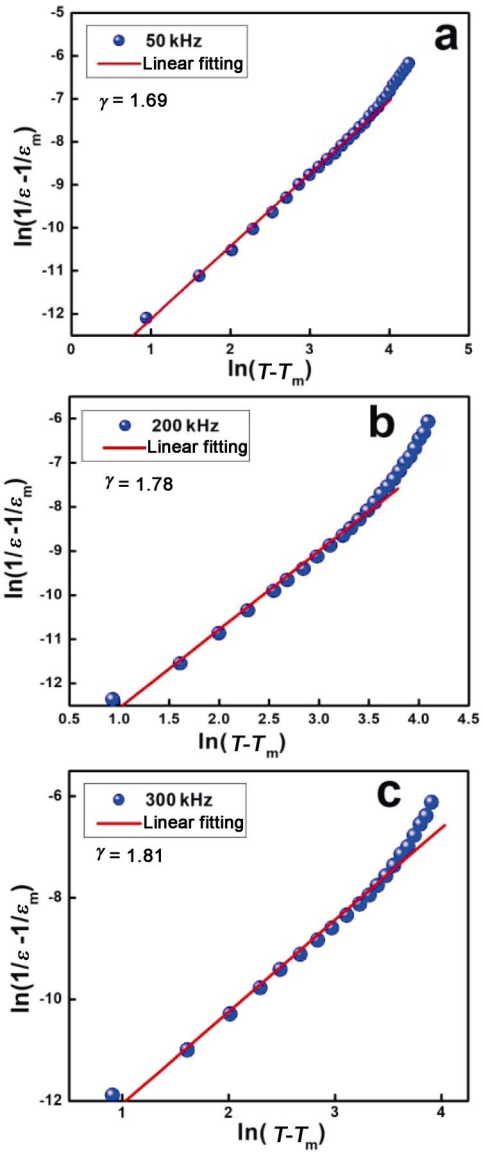

Fig. 3 Variation of $\ln\left(\frac{1}{\varepsilon}-\frac{1}{\varepsilon_{\mathrm{m}}}\right)$ with $\ln(T-T_{\mathrm{m}})$: (a) 50, (b) 200, and (c) 300 kHz.

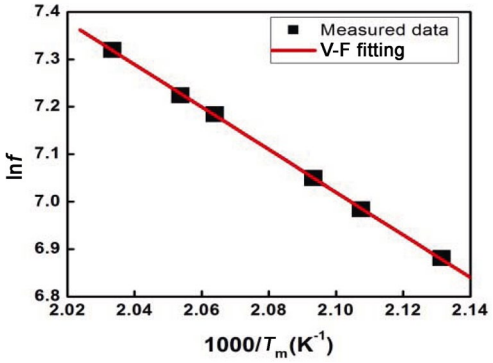

Fig. 4 Dependence of the ln$f$ with $1000/T_{\mathrm{m}}$ (Vogel–Fulcher fitting).

the related to the influence of conductivity due to oxygen vacancies.

3. 4 Impedance spectroscopy

Microstructural and electrical characteristics of the sample were discussed by complex impedance spectroscopy (CIS) method. To know the highest probable information concerning the electrical characteristics of the compound, CIS method is adapted which contains four basic formalisms: impedance, admittance, permittivity, and modulus formalism. Every individual yields a broad extent of graphical investigation relating to these electrical characteristics [22,23]. To differentiate grain, grain boundary, and electrode response of the material, the impedance measurement has been done in the frequency range of 1 kHz–1 MHz and the temperature frequency of 25–300 ℃. The complex impedance (Z^*) has both real (Z') and imaginary (Z'') components.

$$Z^* = Z' + \mathrm{i}Z'' \tag{4}$$

$$Z' = \frac{R}{1+(\omega\tau)^2} \quad \text{and} \quad Z'' = \frac{\omega R\tau}{1+(\omega\tau)^2} \tag{5}$$

where R is the resistance, ω is the angular frequency, and $\tau = RC$ (C is the capacitance) is the relaxation time which can be calculated by the expression $\tau = R_g C_g$ (where, R_g and C_g are the effective resistance and capacitance in parallel). The values of these parameters are given in Table 2. In the Z' vs. frequency graph (Fig. 5(a)), the value of Z' reduces at lower frequencies with an increment of temperature representing rise of AC conductivity and it can also be pointed out that Z' values reduce with the rise of temperature demonstrating the decrease of resistance of grain boundaries, grains, and electrode interface. It represents the negative temperature coeficient resistance (NTCR) nature in the compound. So the semiconductor behavior of the sample is assumed due to fall of Z' with the enhancement of temperature. At higher frequency, all the curves look to be merged representing the existence of space charge in the sample [24].

Table 2 Comparison of calculated values of grain resistance (R_g), grain boundary resistance (R_{gb}), grain capacitance (C_g), grain boundary capacitance C_{gb}, and constant phase factor (Q_g, Q_{gb}) at some selected temperatures

Temperature (℃)	Model	R_g(Ω)	Q_g	C_g (F)	R_{gb}(Ω)	C_{gb}(F)
25	(RQC)	1.971E+004	3.254E–010	7.871E–011	—	—
50	(RQC)	1.059E+004	1.487E–010	5.248E–017	—	—
75	(RQC)	5.805E+003	1.406E–010	9.433E–021	—	—
100	(RQC)	3.359E+003	1.499E–010	1.059E–010	—	—
125	(RQC)	2.016E+003	1.923E–009	1.096E–010	—	—
150	(RQC)	1.191E+003	1.747E–009	1.080E–010	—	—
175	(RQC)	8.301E+002	5.408E–008	1.066E–010	—	—
200	(RQC)(RC)	6.429E+001	1.453E–004	2.087E–024	4.435E+002	1.261E–010
225	(RQC)(RC)	7.135E+001	1.211E–004	1.677E–016	2.577E+002	1.397E–010
250	(RQC)(RQC)	9.570E+001	1.838E–005	2.883E–020	1.327E+002	1.767E–010

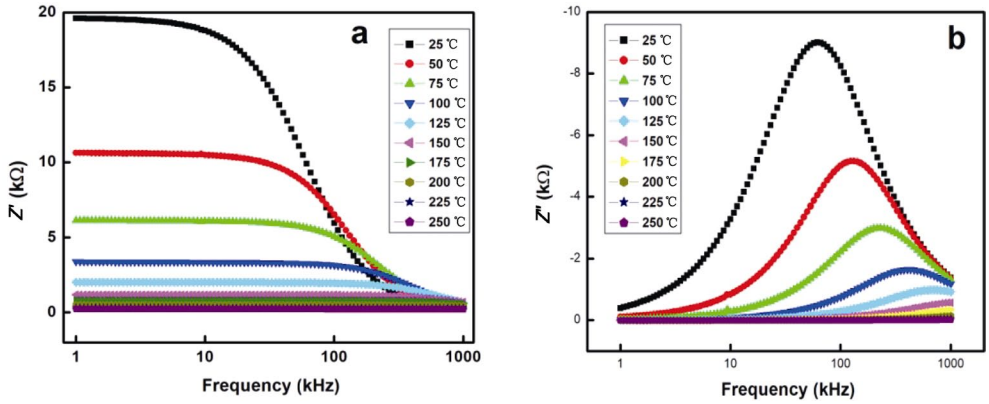

Fig. 5 Variations of (a) Z' and (b) Z'' with frequency at selected temperatures.

In case of Z'' (Fig. 5(b)), the value remains constant up to almost 5 kHz at all temperatures. The sudden increase of Z'' was found due to increase in frequency. At a particular frequency, there is an occurrence of the peak, which is known as relaxation frequency [25]. There is a systematic peak which shifts in the direction of high frequency with an increment of temperature. In the high frequency region, all the values of Z'' start merging, which indicates the accumulation of space charge. The peak position yields the relaxation time by the relation $\omega_{max}\tau = 1$, where ω_{max} is the angular frequency of the Z''_{max} frequency patterns. Due to the broadening and the asymmetry of the peaks, the increment of the distribution of relaxation time and non-Debye-like performance can be obtained in the compound [26]. The relaxation phenomenon arises because of the existence of low-temperature immobile charges and high-temperature defects and vacancies. Such type of behavior is observed not only in perovskite or double perovskite, but also in other oxides of different structural families [27–29].

3. 5 Nyquist plot

The Nyquist plot signifies the variation of Z' with Z'' in the frequency range of 1 kHz–1 MHz and at different temperature of 25–300 ℃ (Fig. 6). The grain, grain boundary, and electrode effects can be understood by a separate semicircular curve in the complex impedance plots. The experimental data were fitted to the resistor and capacitor of an equivalent impedance circuit. According to Debye, in perfect Debye type relaxation, the centre of the semicircles should be coinciding with the real impedance axis. The non-Debye type of relaxation phenomena is observed due to the imperfection of the sample. The parallel RC circuit along with constant phase element represents the deflection from Debye type relaxation. For Debye type relaxation, the test and theoretical data can be calculated by using the software (ZSIMP WIN version 2.0). For 25–175 ℃, the equivalent circuit consists of a single RQC (Q is a constant phase element) circuit and exhibits a single circle representing the contribution comes from grain effect only. For temperature 200–250 ℃, the equivalent circuit consists of a series combination of RQC and RC circuits which comes from the contribution of both grain and grain boundary effect. From Fig. 6(c), the departure of the impedance plane of the real axis by angle of 5.13° at 25 ℃, indicating non-Debye type relaxation in the material.

3. 6 Electrical conductivity

The frequency dependence of AC conductivity (σ_{AC}) has been shown in Fig. 7(a). At any selected temperature, the conductivity has been calculated by the following formula: $\sigma_{AC} = \omega\varepsilon_0\varepsilon_r \tan\delta$ (ω = angular frequency, ε_0 = absolute permittivity, and $\tan\delta$ = tangent loss). The dispersive behavior of the conductivity can be

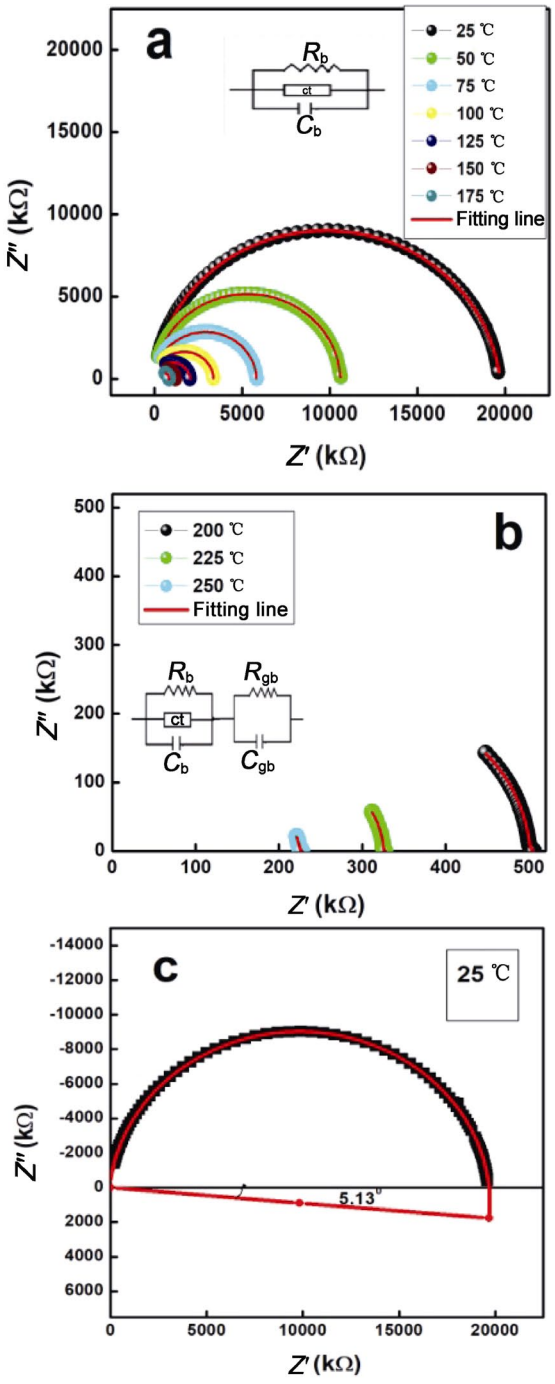

Fig. 6 Variation of Z' with Z'': (a) 25–175 ℃, (b) 200–250 ℃, and (c) 25 ℃ with depression angle.

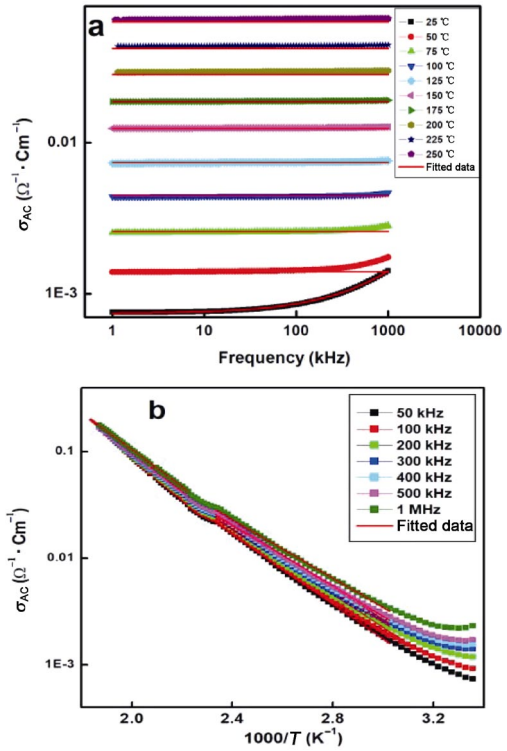

Fig. 7 Variation of AC conductivity with (a) frequency at selected temperatures and (b) inverse of absolute temperatures.

understood by Jonscher's power law, which is given by total conductivity $\sigma_T = \sigma_{DC} + \sigma_{AC} = \sigma_{DC} + A_1 (T)^s$, where σ_{DC} and σ_{AC} are the DC and AC conductivities respectively. The exponent (s) lies between 0 and 1. The pre-exponential factor A_1 is the strength of polarizability which depends on temperature [31–33]. Since, we obtained $n < 1$, so the conduction phenomenon is of non-Debye type. In Fig. 7(a), we have noticed that at very low temperature (25 ℃) and high frequency, the value of AC conductivity slowly increases; otherwise, it remains constant that means it is almost frequency independent. The temperature dependence of σ_{AC} in the frequency range of 50 kHz–1 MHz can be observed by Arrhenius relation [34,35]. According to this relation,

$$\sigma_{AC} = \sigma_0 \, ^{-E_a/kT} \quad (6)$$

$$\text{or} \quad \ln(\sigma_{AC}) = \ln \sigma_0 - E_a/kT \quad (7)$$

where k is the Boltzmann constant and σ_0 is the pre-exponential factor. Using Eq. (6) or (7), AC activation energy has been calculated. This material shows NTCR nature that means there is an increment of conductivity with rise in temperature (Fig. 7(b)). This behavior of AC conductivity represents the existence of thermally activated transport behavior in the sample. In polycrystalline sample, the defects are created at high temperatures. This defect acts as the source of additional acceptor centers. Due to these defects, there is a decrease in activation energy by temperature rising. The estimated values of E_a in both low and high temperatures are shown in Table 3. This estimated activation energy is in good agreement with Ref. [36] for Sm_2NiMnO_6 (formed by a high-temperature solid-state reaction method). The energy essential for the movement of an electron from Ni^{+2} to Mn^{+4} is approximately equal to this determined activation energy.

3.7 Modulus analysis

The study of electrical modulus of compound is extremely essential to observe the electrode effect, grain boundary effect, grain properties, conductivity, and relaxation behavior under the consequence of frequency and temperature. The most significant benefit of such process is to study the existence conduction process and electrical relaxation process in the polycrystalline compound [37]. The frequency dependence of M' (real part) at some selected temperatures has been shown in Fig. 8(a). The M' can be calculated by using the following formula:

$$M' = A\left[\frac{(\omega RC)^2}{1+(\omega RC)^2}\right] = A\left[\frac{(\omega\tau)^2}{1+(\omega\tau)^2}\right] \quad (8)$$

In the low-frequency range, the value of M' (at all temperatures) is small (nearly 0), which represents that there is an absence of effect of electrode and/or ionic polarization. When the frequency increases, the value of M' increases. Such continuous dispersion with an increment of frequency may provide an idea about the

Table 3 Frequency and temperature dependence of activation energy

Frequency	E_a at high temperature (174–266 ℃) (eV)	E_a at low temperature (54–156 ℃) (eV)
50 kHz	0.411	0.324
100 kHz	0.398	0.314
200 kHz	0.383	0.303
300 kHz	0.377	0.295
400 kHz	0.370	0.289
500 kHz	0.364	0.285
1 MHz	0.347	0.272

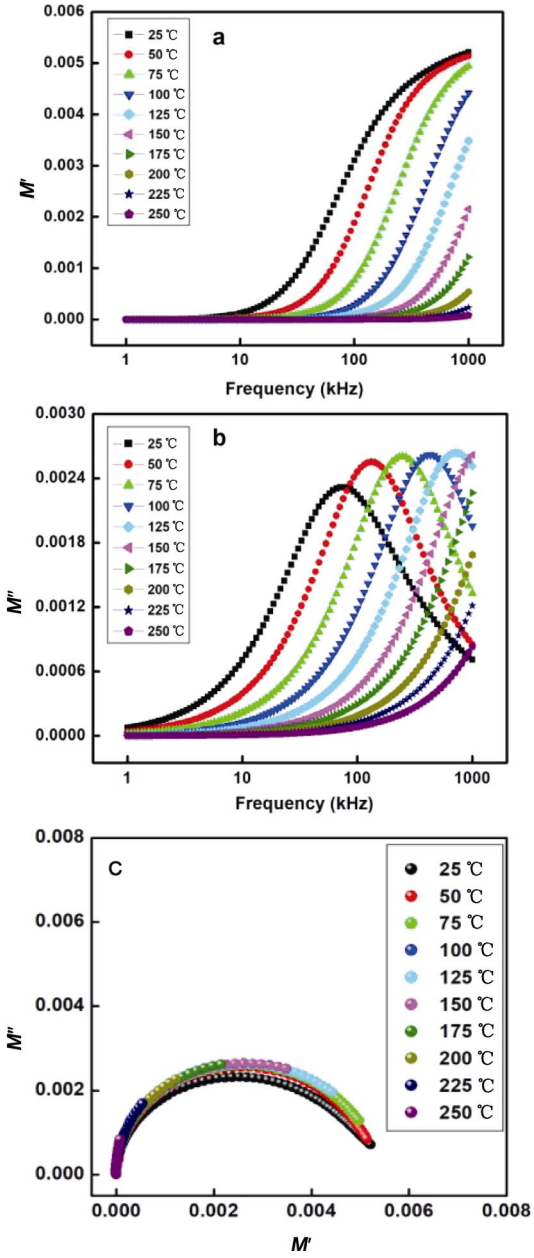

Fig. 8 Variation of (a) M', (b) M'' with frequency at selected temperatures, and (c) variation of M' with M'' at selected temperatures.

conduction process which is owing to the short-range movement of charge carriers. It is probably associated with the absence of restoring force leading to the movement of the charge carriers by the effect of a produced electrifield. Increase of M' with the increment of temperature describes the obtained relaxation phenomena is temperature dependent. The shifting of a dispersion region in the direction of the high-frequency region indicates the long-range movement of charge carriers. The occurrence of higher frequencies plateau proposes the frequency invariant (DC conductivity) electrical characteristics [22]. The curve between M'' (imaginary part) and frequency at some temperatures has been shown in Fig. 8(b). The value of M'' can be calculated as,

$$M'' = A\left[\frac{\omega RC}{1+(\omega RC)^2}\right] = A\left[\frac{\omega\tau}{1+(\omega\tau)^2}\right] \quad (9)$$

The value of M'' rises with an increase in frequency, and attains maximum value (peak). The value of M''_{max} is different for different temperature. As the value of M'' decreases, it suggests the occurrence of relaxation in the sample caused by hopping of charge carriers [38]. With increasing the temperature, the peaks shift in the direction of high-frequency area. The variation of the value of M''_{max} with the temperature yields the variation of capacitance. Above 125 ℃, the broadening of peaks occurs indicating the decreasing of relaxation time of charge carriers.

The study of the complex modulus spectrum (M' vs. M'') at different temperatures is depicted in Fig. 8(c). The occurrence of an arc in the range at a certain temperature suggests the single phase properties of the compound. The obtained higher temperature arcs are not perfectly semicircle. At low frequencies and high temperatures, tail of the curve is not completely developed to its accurate form due to frequency and temperature limitations [39]. The asymmetric semicircular arc confirms the occurrence of electrical relaxation phenomena in the material.

Figure 9(a) displays the relative analysis of the imaginary modulus and impedance (M'' and Z'') with frequency. This plot also supports to study the feedback of less capacitance and large resistance. Besides, it distinguishes between short- and long-range movement of charge carriers. The mismatching of Z''_{max} and M''_{max} peaks suggests the short-range flow of charge carriers, whereas the matching indicates the long-range type charge carriers. As we observed the mismatching of the peaks, short-range type charge carrier and deviation from ideal Debye-like behavior are confirmed [40,41].

Figure 9(b) is represented as the graph of the relaxation time (determined from Z'' and M'' spectroscopy plot) with inverse absolute temperature which followed by Arrhenius law, $\tau_r = \tau_0 \exp(-E_a / K_B T)$. The determined E_a (0.56 eV) from impedance spectroscopy corresponds to localized conduction whereas E_a (0.53 eV) at the same temperature calculated

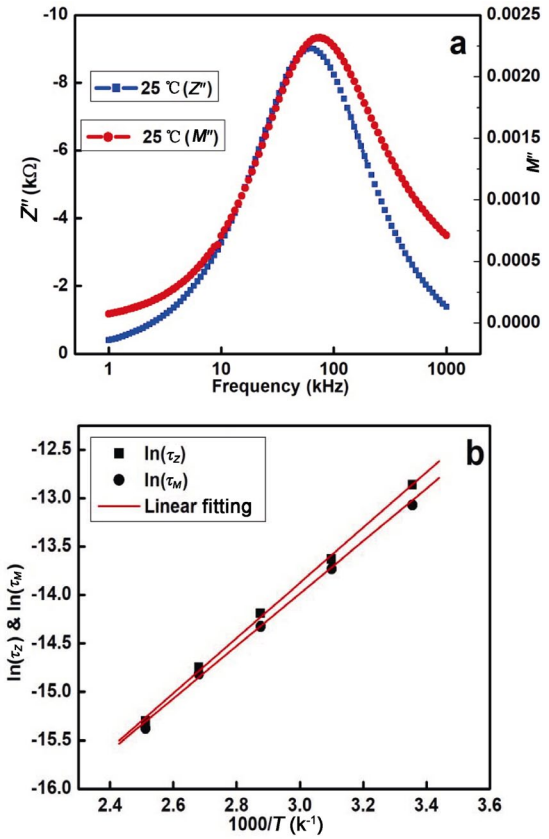

Fig. 9 (a) Graph of M'' and Z'' with frequency at 25 ℃ and (b) $\ln\tau_r$ ($r = Z, M$) vs. $1000/T$ of the studied sample.

from M'' spectra indicates non-localized conduction [42]. Almost equal E_a, calculated from these two spectra, suggested that participating charge carriers were equivalent in both conduction processes.

3. 8 Magnetic properties

Figure 10 depicts the room temperature magnetic hysteresis loop. The magnetic field dependence of magnetization (M–H loop) curve is linear at room temperature (300 K), signifying a complete paramagnetic character. This finding is also supported by Ref. [6].

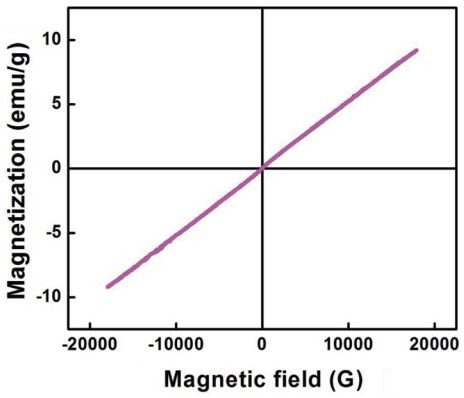

Fig. 10 Room temperature M–H curve.

3. 9 ME properties

ME coupling describes the impact of a magnetic field on the polarization and vice versa [43,44]. Multiferroic ME compounds provide the chance to analyze the unique physical mechanism, and exhibit the probability for their utilization in novel multi-functional materials, such as transducers transforming among magnetic and electric fields, attenuators, filters, field probes, and data recording devices based on the electrical control of magnetization, and vice versa [45]. It may arise directly between the two order parameters or directly via strain. ME voltage coefficient can be obtained as,

$$\alpha_E = \frac{\mathrm{d}E}{\mathrm{d}H} = \frac{V}{h_0 d} \tag{10}$$

where E is the induced electric field, H is the applied magnetic field, V is the magnetoelectric voltage developed across the sample, h_0 is the magnitude of the AC magnetic field, and d is the thickness of the sample. To determine ME coefficient, both AC and DC magnetic fields have been applied simultaneously. The induced voltage across the sample was measured by the lock-in amplifier in the ME setup. This experiment was done in AC magnetic field of 15.37 Oe and 1 kHz frequency along with varying magnitude (–5–5 kOe) of DC magnetic field. The AC field h_0 which is induced in the Helmholtz coil (N = 200 turns, r = 2.5 cm and resistance R = 23.4 Ω) is given by

$$h_0 = \frac{\mu_0}{4\pi}\frac{2\pi NIr^2}{\left(r^2+\frac{r^2}{4}\right)^{3/2}}\times 2 = \frac{\mu_0}{\left(\frac{5}{4}\right)^{3/2}}\left(\frac{NI}{r}\right)$$

$$= 8.99\times10^{-3}\frac{NV}{rR}\,(\mathrm{Oe}) \tag{11}$$

Here 15.37 Oe of the magnetic field was generated by the application of 5 AC amplitude to the Helmholtz coil. Due to the spontaneous magnetization of the sample, even in the zero-magnetic field, there is some magneto- electric voltage coefficient [46,47]. Figure 11 shows that curve between ME voltage coefficient and applied DC magnetic field in Sm_2NiMnO_6 and the ME voltage coefficient is found to be 1.15 $mV\cdot cm^{-1}\cdot Oe^{-1}$ at zero- magnetic field.

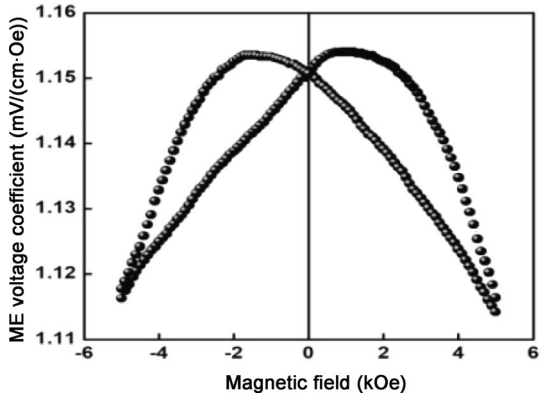

Fig. 11 ME voltage coefficient with the applied DC magnetic field.

4 Conclusions

The polycrystalline sample Sm_2NiMnO_6 was synthesized by a high temperature solid-state reaction technique. The monoclinic structure of the sample was found from X-ray analysis. The crystallite size was found to be 65 nm by Scherrer's formula. The microstructural analysis shows the uniform distribution of grains of different shape and size with small voids over the surface of the sample. The electrical parameters are calculated from dielectric and impedance measurements. In temperature dependence of dielectric property, the value increases and an anomaly was observed at a certain temperature. Then the value of dielectric constant was found to be decreased. This sample has higher dielectric constants due to the combination of conducing grain and insulating grain boundary. In the Nyquist plot, it was found that for temperature 25–175 ℃, circles are made by only single RQC network representing the existence of grain effect. At high temperature (200–250 ℃), the polarization exhibits by the simultaneous occurrence of grain and grain boundary effect that represented by the series combination of RQC and RC circuit. From the study of complex impedance spectroscopy, the non-Debye type of dielectric relaxation was confirmed. The semiconductor behavior of the sample was obtained from the conductivity versus temperature. The room temperature magnetic hysteresis loop shows the paramagnetic behavior. From the ME property, ME voltage coefficient is found to be 1.15 $mV{\cdot}cm^{-1}{\cdot}Oe^{-1}$. This type of lead free relaxor ferroelectric compound may be used for different high temperature applications. In conclusion, the sample Sm_2NiMnO_6 can be used in different modern electronic devices.

Acknowledgements

The authors would like to extend their gratitudes and sincere thanks to Dr. Kalyani Mohanta, Indian Institute of Technology, BHU, for providing some experimental facilities for microstructure and Dr. Perumal Alagarsamy, Indian Institute of Technology, Guwahati, providing the experimental facility for magnetic measurements.

References

[1] Sahoo S, Mahapatra PK, Choudhary RNP. The structural, electrical and magnetoelectric properties of soft-chemically-synthesize $SmFeO_3$ ceramics. *J Phys D: Appl Phys* 2016, **49**: 035302.

[2] Parida K, Dehury SK, Choudhary RNP. Structural, electrical and magneto-electric characteristics of $BiMgFeCeO_6$ ceramics. *Phys Lett A* 2016, **380**: 4083–4091.

[3] Ortega N, Kumar A, Scott JF, *et al*. Multifunctional magnetoelectric materials for device applications. *J Phys: Condens Matter*, 2015, **27**: 504002.

[4] Singh DN, Sinha TP, Mahato DK. Structural and dielectric characteristics of La_2CuMnO_6 double perovskite ceramics. *Mater Today-Proc* 2017, **4**: 5640–5646.

[5] Bartesaghi D, Slavney AH, Gélvez-Rueda MC, *et al*. Charge carrier dynamics in Cs_2 $AgBiBr_6$ double perovskite. *J Phys Chem C* 2018, **122**: 4809–4816.

[6] Gheorghiu F, Curecheriu L, Lisiecki I, *et al*. Functional properties of Sm_2NiMnO_6 multiferroic ceramics prepared by spark plasma sintering. *J Alloys Compd* 2015, **649**: 151.

[7] Reshak AH, Azam S. Electronic band structure and specific features of Sm_2NiMnO_6 compound: DFT calculation. *J Magn Magn Mater* 2013, **342**: 80.

[8] Blasse G. Ferromagnetic interactions in non-metallic perovskites. *J Phys Chem Solids* 1965, **26**: 1969–1971.

[9] Khandy SA, Gupta DC. Electronic structure, magnetism and thermoelectric properties of double perovskite Sr_2HoNbO_6. *J Magn Magn Mater* 2018, **458**: 176–182.

[10] Khandy SA, Gupta DC. Electronic structure, magnetism and thermoelectricity-in layered perovskites: Sr_2SnMnO_6 and Sr_2SnFeO_6. *J Magn Magn Mater* 2017, **441**: 166–173.

[11] Fan HQ, Ke SM. Relaxor behavior and electrical properties of high dielectric constant materials. *S Sci China Ser E-Technol Sci* 2009, **52**: 2180–2185.

[12] Cross LE. Relaxor ferroelectrics. *Ferroelectrics* 1987, **76**: 241–267.

[13] Parida B N, Panda N, Padhee R, *et al*. Dielectric relaxation and impedance analysis of ferroelectric double perovskite Pb_2BiNbO_6. *J Mater Sci: Mater Electron* 2017, **28**: 1824–1831.

[14] Lekshmi P, Raji GR, Vasundhara M, *et al*. Re-entrant spin glass behaviour and magneto-dielectric effect in insulating Sm_2NiMnO_6 double perovskite. *J Mater Chem C* 2013, **1**: 6565–6574.

[15] Shi C Y, Hao Y M, Hu ZB. Local valence and physical properties of double perovskite Nd_2NiMnO_6. *J Phys D: Appl Phys* 2011, **44**: 245405.

[16] Bokov AA, Ye ZG. Dielectric relaxation in relaxor ferroelectrics. *J Adv Dielect* 2012, **2**: 1241010.
[17] Burns G, Dacol FH. Crystalline ferroelectrics with glassy polarization behaviour. *Phys Rev B* 1983, **28**: 2527.
[18] Glazounov AE, Tagantsev AK. Direct evidence for Vogel–Fulcher freezing in relaxor ferroelectrics. *Appl Phys Lett* 1998, **73**: 856.
[19] Vugmeister BE, Glinichuk MD. Dipole glass and ferroelectricity in random-site electric dipole systems. *Rev Mod Phys* 1990, **62**: 993–1026.
[20] Sliwinska-Bartkowiak M, Dudziak G, Sikorski R, *et al*. Dielectric studies of freezing behavior in porous materials: water and methanol in activated carbon fibres. *Phys Chem Chem Phys* 2001, **3**: 1179–1184.
[21] Du HL, Zhou WC, Luo F, *et al*. Phase structure, dielectric properties, and relaxor behavior of $(K_{0.5}Na_{0.5})NbO_3$–$(Ba_{0.5}Sr_{0.5})TiO_3$ lead-free solid solution for high temperature applications. *J Appl Phys*2009, **105**: 124104.
[22] Ranjan R, Kumar R, Kumar N, *et al*. Impedance and electric modulus analysis of Sm-modified Pb $(Zr_{0.55}Ti_{0.45})_{1-x}/4O_3$ ceramics. *J Alloys Compd* 2011, **509**: 6388–6394.
[23] Paiva DVM, Silva MAS, Sombra ASB, *et al*. Dielectric investigation of the Sr_3WO_6 double perovskite at RF/ microwave frequencies. *RSC Adv* 2016, **6**: 42502–42509.
[24] Mahato DK, Dutta A, Sinha TP. Impedance spectroscopy analysis of double perovskite Ho_2NiTiO_6. *J Mater Sci* 2010, **45**: 6757–6762.
[25] Parida K, Dehury SK, Choudhary RNP. Structural, electrical and magneto-electric characteristics of complex multiferroic perovskite $Bi_{0.5}Pb_{0.5}Fe_{0.5}Ce_{0.5}O_3$. *Journal Mate Sci: Mater Electron*, 2016, **27**: 11211–11219.
[26] Pradhan D K, Choudhary R N P, Rinaldi C, *et al*. Effect of Mn substitution on electrical and magnetic properties of $Bi_{0.9}La_{0.1}FeO_3$. *J Appl Phys* 2009, **106**: 024102.
[27] Parida BN, Das PR, Padhee R, *et al*. A new ferroelectric oxide $Li_2Pb_2Pr_2W_2Ti_4Nb_4O_{30}$: Synthesis and characterization. *J Phys Chem Solids* 2012, **73**: 713–719.
[28] Barick BK, Choudhary RNP, Pradhan DK. Dielectric and impedance spectroscopy of zirconium modified $(Na_{0.5}Bi_{0.5})TiO_3$ ceramics. *Ceram Int* 2013, **39**: 5695–5704.
[29] Pattanayak S, Parida BN, Das PR, *et al*. Impedance spectroscopy of Gd-doped $BiFeO_3$ multiferroics. *Appl Phys A* 2013, **112**: 387–395.
[30] Gupta P, Padhee R, Mahapatra P K, *et al*. Structural, dielectric, impedance and modulus spectroscopy of $Bi_2NdTiVO_9$ ferroelectric ceramics. *J Mater Sci: Mater Electron* 2017, **28**: 17344–17353.
[31] Deepti PL, Patri K, Choudhary RNP. $MgBi_2V_2O_9$: Preparation and electrical property evaluation. *J Mater Sci: Mater Electron* 2017, **28**: 16071–16076.
[32] Padhee R, Das PR, Parida BN, *et al*. Structural, dielectric and electrical properties of dysprosium based new complex electroceramics. *J Mater Sci: Mater Electron* 2012, **23**: 1688–1697.
[33] Choudhary RNP, Pradhan DK, Tirado CM, *et al*. Effect of La substitution on structural and electrical properties of $Ba(Fe_{2/3}W_{1/3})O_3$ nanoceramics. *J Mater Sci* 2007, **42**: 7423–7432.
[34] Purohit V, Padhee R, Choudhary RNP. Dielectric and impedance spectroscopy of $Bi(Ca_{0.5}Ti_{0.5})O_3$ ceramic. *Ceram Int* 2018, **44**: 3993–3999.
[35] Sutar BC, Pati B, Parida BN, *et al*. Dielectric and impedance characteristics of $Ba(Bi_{0.5}Nb_{0.5})O_3$ ceramics. *J Mater Sci: Mater Electron* 2013, **24**: 2043–2051.
[36] Yang WZ, Liu XQ, Zhao HJ, *et al*. Structure, magnetic, and dielectric characteristics of Ln_2NiMnO_6 (Ln = Nd and Sm) ceramics. *J Appl Phys* 2012, **112**: 064104.
[37] Parida BN, Padhee R, Suara D, *et al*. Multiferroic and conduction characteristics of $(Bi_{0.5}Ba_{0.5})(Fe_{0.5}Ti_{0.5})O_3$ solid solution. *J Mater Sci Mater Electron* 2016, **27**: 9015–9021.
[38] Paiva DVM, Silva MAS, Sombra ASB, *et al*. Properties of the Sr_3MoO_6 electroceramic for RF/microwave devices. *J Alloys Compd* 2018, **748**: 766–773.
[39] Patri SK, Choudhary RNP. Electrical properties of $LaBi_8Fe_5Ti_3O_{27}$. *J Mater Sci: Mater Electron* 2008, **19**: 1240–1246.
[40] Sinclair DC, West AR. Impedance and modulus spectroscopy of semiconducting $BaTiO_3$ showing positive temperature coefficient of resistance. *J Appl Phys* 1989, **66**: 3850–3856.
[41] Kumar N, Patri SK, Choudhary RNP. Characterization of $Bi_4Pb_2Ti_3FeNbO_{18}$ nanoplates. *J Alloys Compd* 2014, **615**: 456–460.
[42] Jonscher AK. Dielectric relaxation in solids. *J Phys D: Appl Phys* 1999, **32**: R57–R70.
[43] Schimd H. Multi-ferroic magnetoelectrics. *Ferroelectric* 1994, **162**: 317–338.
[44] Martins P, Moya X, Phillips LC, *et al*. Linear anhysteretic direct magnetoelectric effect in $Ni_{0.5}Zn_{0.5}Fe_2O_4$/poly (vinylidene fluoride-trifluoroethylene) 0-3 nanocomposites. *J Phys D: Appl Phys* 2011, **44**: 482001.
[45] Gil K, Gil J, Cruz B, *et al*. Experimental set up of a magnetoelectric measuring system operating at different temperatures. *J Phys Conf Ser* 2016, **687**: 01209.
[46] Shi M, Zuo R, Xun Y, *et al*. Preparation and multiferroic properties of 2-2 type $CoFe_2O_4$/$Pb(Zr,Ti)O_3$ composite films with different structures. *Ceram Int* 2014, **40**: 9249–9256.
[47] Dipti, Juneja JK, Singh S, *et al*. Enhancement in magnetoelectric coupling in PZT based composites. *Ceram Int* 2015, **41**: 6108–6112.